Accepted Manuscript

Substrate-induced strain in carbon nanodisks

Z. Osváth, Z. Vértesy, J. Lábár, P. Nemes-Incze, Z.E. Horváth, L.P. Biró

PII: S0040-6090(14)00723-8
DOI: doi: 10.1016/j.tsf.2014.07.002
Reference: TSF 33569

To appear in: *Thin Solid Films*

Received date: 18 February 2014
Revised date: 30 June 2014
Accepted date: 2 July 2014

Please cite this article as: Z. Osváth, Z. Vértesy, J. Lábár, P. Nemes-Incze, Z.E. Horváth, L.P. Biró, Substrate-induced strain in carbon nanodisks, *Thin Solid Films* (2014), doi: 10.1016/j.tsf.2014.07.002

Substrate-induced strain in carbon nanodisks

Z. Osváth[1,2,*], Z. Vértesy[1,2], J. Lábár[1], P. Nemes-Incze[1,2], Z. E. Horváth[1,2], and L. P. Biró[1,2]

[1]*Institute of Technical Physics and Materials Science, MFA, Research Centre for Natural Sciences, 1525 Budapest, P.O. Box 49, Hungary (http://www.nanotechnology.hu/)*

[2]*Korea-Hungary Joint Laboratory for Nanosciences (KHJLN), P.O. Box 49, 1525 Budapest, Hungary*

Abstract:

Graphitic nanodisks of typically 20 – 50 nm in thickness, produced by the so-called Kvaerner Carbon Black and Hydrogen Process were dispersed on gold substrate and investigated by atomic force microscopy (AFM), field emission scanning electron microscopy (FE-SEM), and confocal Raman spectroscopy. The roughness of the gold surface was drastically changed by annealing at 400 ^{o}C. AFM measurements show that this change in the surface roughness induces changes also in the topography of the nanodisks, as they closely follow the corrugation of the gold substrate. This leads to strained nanodisks, which is confirmed also by confocal Raman microscopy. We found that the FE-SEM contrast obtained from the disks depends on the working distance used during the image acquisition by In-lens detection, a phenomenon which we explain by the decrease in the amount of electrons reaching the detector due to diffraction. This process may affect the image contrast in the case of other layered materials, like hexagonal boron nitride, and other planar hybrid nanostructures, too.

* Corresponding author. Tel: +36 1 392 2222 / 3616. E-mail: osvath.zoltan@ttk.mta.hu (Zoltán Osváth).

1. Introduction

Industrial amounts of carbon nanodisks can be produced by the so-called Kvaerner Carbon Black & Hydrogen Process (CBH) [1], which decomposes hydrocarbons directly into carbon and H_2, based on a specially designed plasma torch [2]. The solid output of this pyrolytic method consists of nanocones (20%) [3], a large number of carbon nanodisks (70%), and carbon black (10%). The properties of this relatively new material have not yet been fully investigated. Several studies focus on the structural characterization of the nanocones [1, 3, 4] which have well-defined symmetry exclusively determined by the topology at the cone tip. Such nanocones form when several carbon pentagons incorporate into the atomic structure, determining the angle of the cones. Nevertheless, the nanostructures which occur most frequently in the samples produced by the CBH method are the carbon nanodisks. Transmission electron microscope and electron diffraction studies reveal that these disks have multi-layered, graphitic structures [5]. In this study we focus on the characterization of the carbon nanodisks by atomic force microscopy (AFM), field emission scanning electron microscopy (FE-SEM), and confocal Raman spectroscopy. We show that the disks can bend and form curved sheets by following the morphology of the underlying substrate. Surface engineering the structure of two-dimensional membranes is an emerging field which is currently intensely studied with respect to graphene sheets [6, 7]. During the FE-SEM investigation of the carbon nanodisks we observed a contrast anomaly which we think is likely to be observed also in the case of other layered nanoscale crystalline materials, like hexagonal boron nitride (h-BN), or hybrid nanostacks of graphene/h-BN [8].

2. Experimental details

As-grown samples of carbon nanodisks and nanocones produced by the CBH method were obtained from n-TEC (Norway). Isopropyl alcohol and ultrasonic treatment (70 W) was used to suspend the material at a concentration of 0.1 mg/ml. Droplets from the suspension were dispersed on a gold surface which was prepared by depositing Cr/Au (5/300 nm) on a Si wafer. Carbon nanodisks were first identified by optical microscopy and topographic measurements were performed by tapping mode AFM using a Nanoscope IIIa operating in air. AFM cantilevers from Nanosensors were used (PPP-NCHR), with tip radius of curvature of less than 10 nm. The sample was annealed at 400 ^{o}C in air using an electric furnace with quartz tube of 18 mm inner diameter. We used a WITec alpha300 RSA+ instrument for confocal Raman imaging and excitation lasers of 633 nm and 488 nm. FE-SEM observations were performed in a LEO 1540XB microscope with In-lens detector, using an operating voltage of 3 kV. In order to investigate the same nanodisks before and after annealing, we marked the sample substrate with crossing lines using pointed tweezers. Then we chose to investigate nanodisks positioned close to line crossings, which could be easily identified in the combined optical microscope – AFM system we used.

3. Results and discussion

The AFM characterization of the substrate shows that the deposited gold film (Figure 1a) has a surface with root mean square roughness (RMS) of 2.7 nm. After heating the sample at 400 ^{o}C the roughness of the gold surface changed significantly due to surface diffusion of gold particles. This produced a wavy surface (see Figure 1b) with peak-to-peak distances of

several tens of nanometers and in some regions even hundred nanometers. The RMS increased to 48.1 nm. This effect is similar to the roughening observed in annealed Au thin films [9, 10]. AFM measurements performed on the nanostructures supported by the as-deposited gold substrate revealed that in most cases the carbon nanodisks are not completely flat. We observed frequently that they have bent structures. For example, the nanodisk in Figure 2a shows significant upward bending in the vertical direction (light coloured upper part of the nanodisk). In horizontal direction the nanodisk is flatter and here we measure a thickness of approximately 30 nm. It is interesting that the surface morphology formed during annealing modulates the topography of carbon disks too, which follow closely the hills and valleys of the underlying gold surface. This is illustrated in Figure 2b which is the AFM image of the same nanodisk as in Fig. 2a, acquired after annealing. One observes that the topography of the disk changed completely. This means that the surface imparts a strain to the disk which produces a deformation of 8 – 9%. This deformation was determined from the ratio between the vertical (H) and the horizontal (L) distances measured between the markers in Fig. 2b. The nanodisk appears to have sunk partially into the surface, due to the diffusion of gold particles which had built up at the perimeter of the disk upon annealing. A similar effect is shown in Figure 2c-d, where two partially overlapping nanodisks are observed. Here, carbon black particles of about 100 nm in diameter were sitting on the surface of the disks, which were quite mobile and introduced instabilities in the AFM image in Fig. 2c. Figure 2d shows the two nanodisks after annealing. One can observe the rough, wavy gold surface and also that the larger carbon black particle was pushed away, probably by the AFM tip. We focus on the smaller diameter nanodisk, labelled *2*, which suffered a significant topographic distortion upon heating: the surface reconstruction of gold compressed the disk and produced a depression in the centre of the disk. The total deformation is as high as 22% (H/L), 2.4 times larger than its initial deformation.

After annealing we measured the disks shown in Fig. 2 by confocal Raman microscopy. Figures 2e and 2f show the spectral distribution of the *G* peak centre (ω_G) determined by Lorentz fitting to the Raman spectra. Comparing these maps to Fig. 2b and 2d, respectively, we find good correlations with the topographic images. The spectra collected from topographic valleys show *G* peaks at higher wavenumbers whereas these peaks appear at wavenumbers closer to the equilibrium value of the *G* peak (ω_G^o = 1582 cm^{-1}) when measured on hills. The maximal shifts from ω_G^o are 9 cm^{-1} for Fig. 2e and 12 cm^{-1} for Fig. 2f (disk no. *2*), which correspond to a maximal compressive strain ($\Delta\varepsilon$) of -0.16 % and -0.21 %, respectively, if we neglect peak shifts induced by doping inhomogeneity. Here we used the equation $\Delta\varepsilon = -\Delta\omega_G/(2\omega_G^o\gamma_G)$ [11], where $\gamma_G = 1.8$ is the Grüneisen parameter of the *G* peak obtained by the first-principles calculations [12]. We do not observe pronounced *2D* peaks for the carbon disks in Fig. 2. However, we can estimate the maximal strain also from the maximal shift of the *D* peak spectral centre ($\Delta\omega_D$) which is 14 cm^{-1} and 17 cm^{-1}, respectively. Here we consider the equilibrium value of the *D* peak ω_D^o = 1315 cm^{-1}. Using $\Delta\varepsilon = -\Delta\omega_D/(2\omega_D^o\gamma_D)$, and $\gamma_D = 2.3$ [11] we obtain strain values of -0.23% and -0.28%, respectively, which are higher than the ones determined from the shift of the *G* peaks. The difference originates from the fact that the spectral position of the *G* and *D* peaks is not only due to strain but also to doping. We show in Figure 2g the correlation plot (ω_G, ω_D) between the two Raman modes, for both nanodisks labelled *1*, and *2*. These values were extracted from the individual spectra measured on the disks. We also plotted the slopes ($\Delta\omega_D/\Delta\omega_G$) corresponding to variations induced by strain only (solid line) and by purely doping effects (dotted line), respectively. These two slopes intersect each other at the equilibrium values (ω_G^o, ω_D^o). For the strain slope we assumed ($\Delta\omega_D/\Delta\omega_G$) = 1.1, which is half the value of 2.2 obtained in Ref. 13 for ($\Delta\omega_{2D}/\Delta\omega_G$), where the shift of the *2D* peak ($\Delta\omega_{2D}$) was considered. As for the slope indicating pure doping we used ($\Delta\omega_D/\Delta\omega_G$) = 0.375, again considering half

the slope of ($\Delta\omega_{2D}/\Delta\omega_G$) = 0.75 for hole doping induced by electrical gating [13]. This approach is true in a first approximation, because the D peak involves scattering off one phonon around the K point, whereas the 2D peak involves two phonon scattering events [11]. Thus any changes to the phonon frequencies are larger by a factor of 2 in the case of the 2D mode with respect to the D mode. The correlation plot clearly shows that the distribution of peaks measured on the carbon nanodisks is due to a combination of both strain and doping effects. A point on the correlation plot which is closer to the solid line means that the shift is mainly caused by strain. On the other hand, a point which is close to the dotted line shows dominant doping effects. In order to determine which effect changes more significantly when the sample is annealed we performed confocal Raman imaging on a nanodisk both before and after annealing. The corresponding maps of ω_G are presented in Fig. 3a-b. One can observe that the distribution of the *G* peak positions changed upon annealing. Similar change is observed also for the *D* peak positions, ω_D (not shown). On the correlation plot (ω_G, ω_D) in Fig. 3c we observe that the distribution of the peaks shifted towards higher wavenumbers and this shift is mainly parallel to the strain slope. The majority of the points (red circles) are closer to the solid line, which shows that upon annealing the variation in strain is the dominant effect. The shift of the peaks can be also observed on the averaged Raman spectra shown in Figure 3d (see for example the inset which is a zoom on the *G* peak). Furthermore, the spectra reveal that the intensity of the *D* peak is comparable to the one of the *G* peak, indicating important disorder in the graphitic structure of the nanodisk. Similar *D* peak intensities were measured on other nanodisks as well, thus the spectra in Fig. 3d can be considered as typical for the as-grown material. Worthy to note that apart from shifting the peak positions, annealing at moderate temperatures (up to 400 ^{o}C) do not induce significant change in the intensity ratio between the *D* and *G* peaks. This intensity ratio can be related to

the coherence length L_a, which shows the lateral extension of the monocrystalline graphitic domains [14, 15]:

$$L_a(nm) = 10.3 \frac{I_G}{I_D} \qquad (1)$$

According to Eq. (1), we obtain L_a = 3.9 nm, comparable with previous works [15, 16]. AFM measurements performed in a scan window of 350×350 nm^2 on the surface of a nanodisk are shown in Figure 4. Interestingly, the phase image shows small domains of 5 – 20 nm in diameter (Fig. 4b, light-coloured spots) where the phase signal changes significantly. We attribute these changes in the phase to the presence of both crystalline and less crystalline (amorphous) regions that are separated from each other, which is in accordance with the structure determined from X-ray diffraction and Raman spectroscopy [16].

The carbon nanodisk sample dispersed on gold surface was also investigated by FE-SEM. A typical nanodisk is shown in the images of Figure 5a-b which were measured after annealing. We observe a mixture of dark and light regions on the area surrounding the nanodisk, which we label *A*- and *B*-type regions, respectively. These features are actually everywhere on the sample and they originate from the significant modification of surface roughness upon annealing. In-situ energy-dispersive X-ray spectroscopy (EDX) measurements reveal that in the *A*-type regions the Cr signal is more intense due to a thinner gold layer. On the other hand the *B*-type regions correspond to thick gold surface. Furthermore, we label with *C* the nanodisk regions lying on top of the thick gold. Interestingly, the image contrast given by the nanodisk changes with the working distance (WD) of the SEM observation, when using the In-lens detector. While for WD = 6.5 mm the nanodisk is the darkest region in the image (Fig. 5a), it gives almost no contrast to region *B*, i.e. it appears transparent when WD is decreased to 2.3 mm (Fig. 5b). The alteration of the contrast is shown in Figure 5c, where we plotted the contrast ratio *B/C* (greyscale numeric values) between the gold surface not covered by the nanodisk (*B*) and the surface inside the

nanodisk (*C*) as function of WD. For comparison, we also plotted the ratio between *B*- and *A*-type regions (*B*/*A*). We assume that the observed change in the contrast is related to the crystalline layers of the nanodisk, which diffract the secondary electrons (SEs) contributing to the image formation. These electrons reach the In-lens detector through the hole of the pole piece cup (PPC) of the objective lens, which has 5 mm in diameter. Hence, we can estimate the spatial angle of electron collection for each WD. Choosing WD_1 = 6.5 mm and WD_2 = 2.3 mm, the corresponding angles are $\vartheta_1 = 21°$ and $\vartheta_2 = 47.4°$, respectively.

Electron diffraction occurs according to the Bragg equation $2dsin(\vartheta) = \lambda$, where d is the distance between the diffracting crystallographic planes and λ is the de Broglie wavelength of the electrons. In the case of graphitic layers one has to take into account two planes characterized by Miller indices {100} and {110}. The corresponding distances are d_{100} = 2.132 Å and d_{110} = 1.23 Å. Using d_{100} in the Bragg equation we obtain $\lambda_1 = 1.53$ Å for ϑ_1 and $\lambda_2 = 3.14$ Å for ϑ_2. Considering $\lambda = h/\sqrt{2mE}$ this gives electron energies of $E_1 = 64.3\ eV$ and $E_2 = 15.3\ eV$, respectively. It is known that the majority of SEs have energies below 50 eV, with a maximum at around 20 eV, and a small part of electrons with energies between 50 and 100 eV [17]. This means that there is significant number of SEs having energies between E_1 and E_2 which can diffract on the carbon nanodisk. In the case of small WD (WD_2 = 2.3 mm), these low energy SEs reach easily the detector. In contrast, for WD_1 = 6.5 mm diffracted electrons with energies less than E_1 do not reach the hole of the PPC and practically they are not collected. As a result, the nanodisk appears darker in the FE-SEM images obtained at WD_1 = 6.5 mm. Note that the contrast ratio between *B*- and *A*-type regions is nearly constant. This is consistent with our interpretation because no diffraction is assumed outside the nanodisk. In the case of diffraction on the plane {110} with d_{110} = 1.23 Å only the electrons with energies higher than 193 eV enter the PPC for WD_1 = 6.5 mm. However, neither backscattered nor secondary electrons are present in significant number in this energy

range. Nevertheless, for WD_2 = 2.3 mm diffracted electrons with energies higher than E = 46 eV do enter the PPC and they contribute to the image contrast. Note that the observed variation of the FE-SEM contrast is different from the WD dependent contrast change observed in a low vacuum SEM when charging insulating glass spheres [18]. Our observation may have importance not only for graphitic stacks, but also for other two-dimensional layered materials like thin h-BN platelets, vertically stacked graphene/h-BN, or graphene/MoS_2/metal complex nanoarchitectures [19].

4. Conclusions

We have shown by AFM measurements that carbon nanodisks can significantly deform as they follow the surface roughness changes of gold substrate induced by annealing. This leads to strained nanodisks, which is confirmed also by confocal Raman microscopy. They support deformations as high as 22 %, which makes them interesting alternative candidates for fillers in composite materials. We observed that the FE-SEM contrast obtained from the disks depends on the working distance at which the image was obtained. We explain this finding by the diffraction of the secondary electrons on the graphitic structure, which decreases the amount of electrons reaching the detector. This contrast alteration is likely to be observable also during the FE-SEM investigation with In-lens detection of other nanoscale crystalline materials forming homogenous or heterogenous two-dimensional nanostacks.

Acknowledgements

The research leading to these results has received funding from the Korea-Hungary Joint Laboratory for Nanosciences and the People Programme (Marie Curie Actions) of the European Union's Seventh Framework Programme (FP7/2007-2013) under REA grant

agreement n° 334377. The authors acknowledge the financial support from OTKA Grant K 101599. Z.O. acknowledges the János Bolyai Research Fellowship from the Hungarian Academy of Sciences.

References

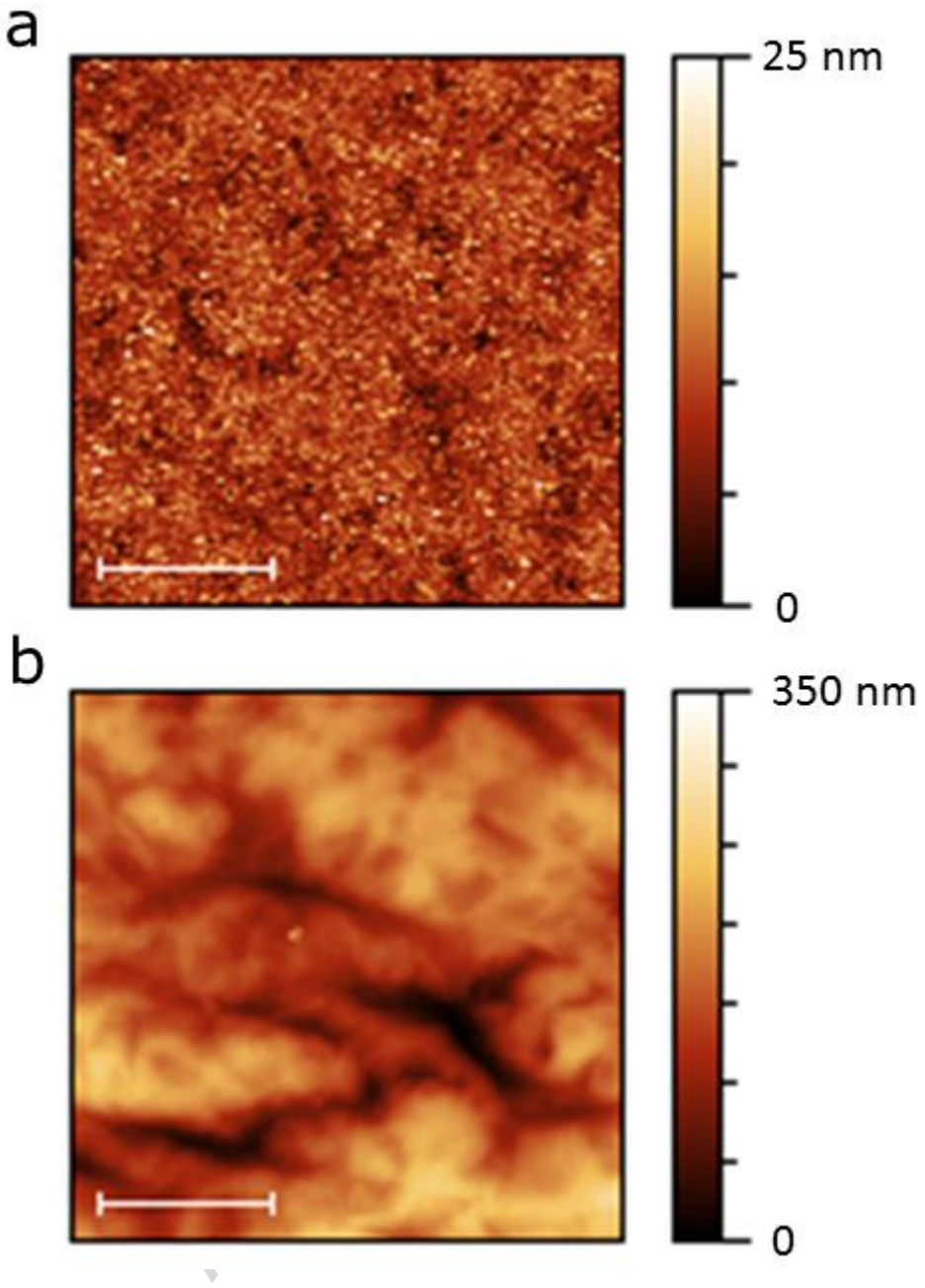

Figure1

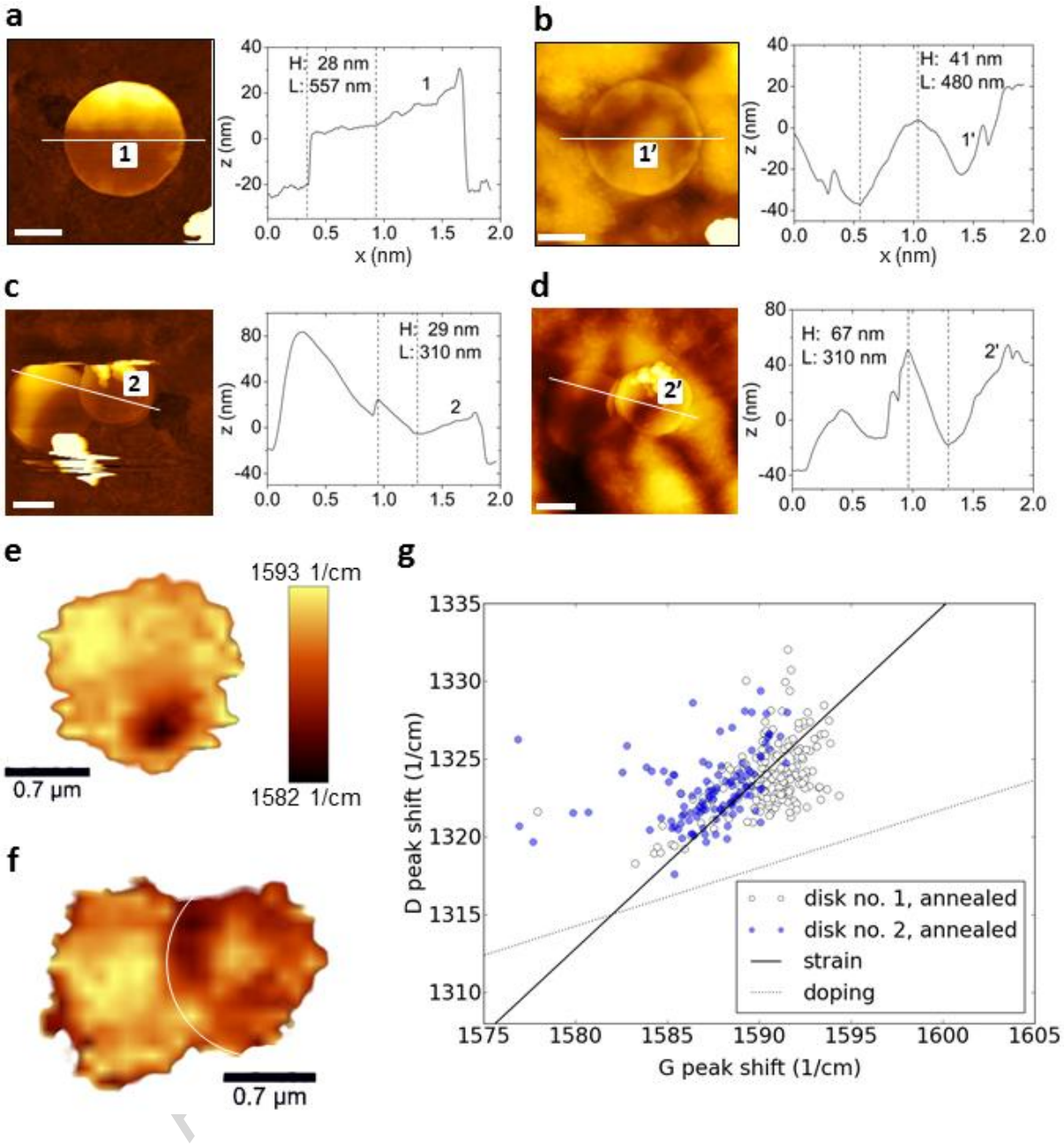

Figure2

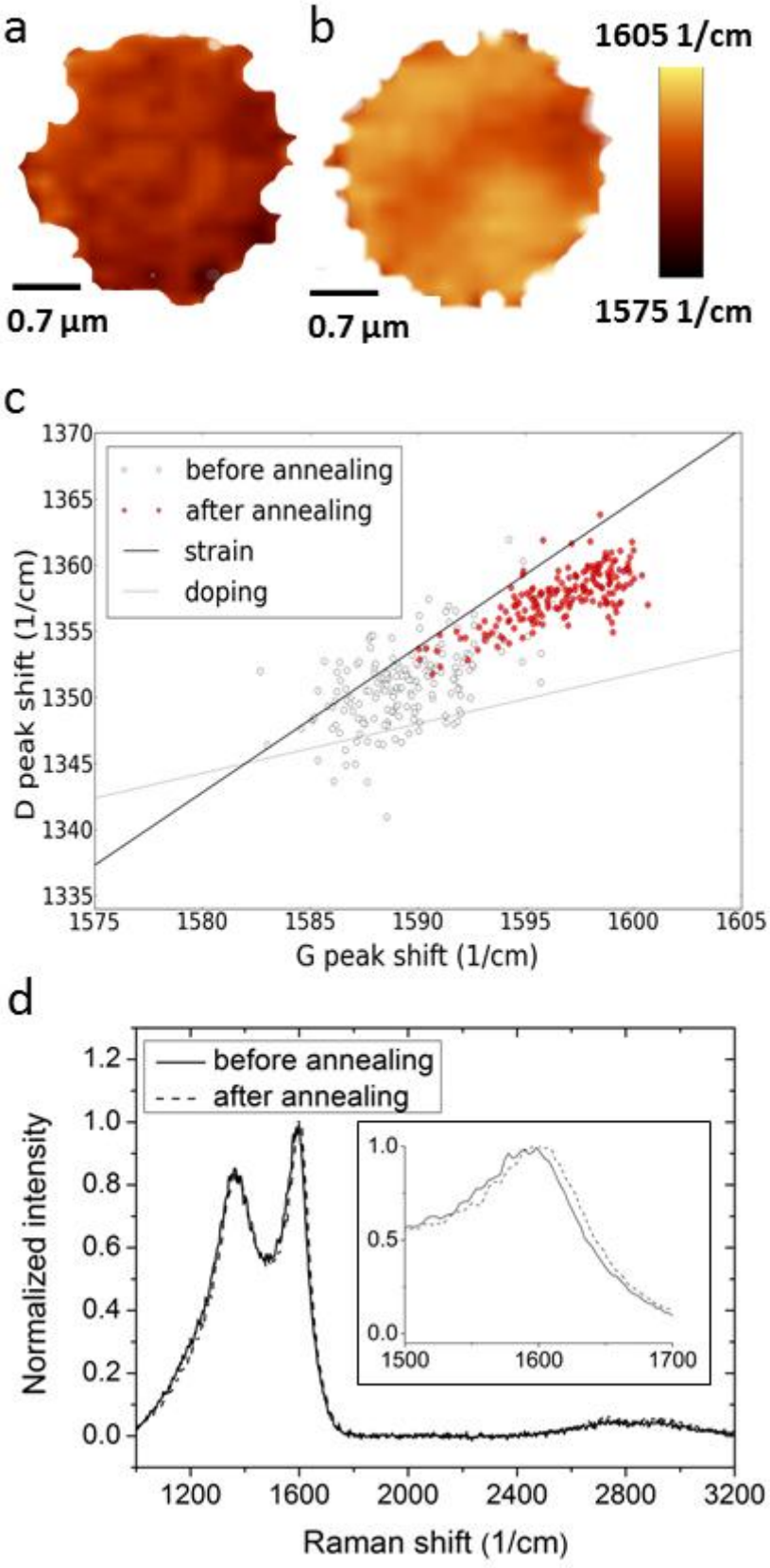

Figure3

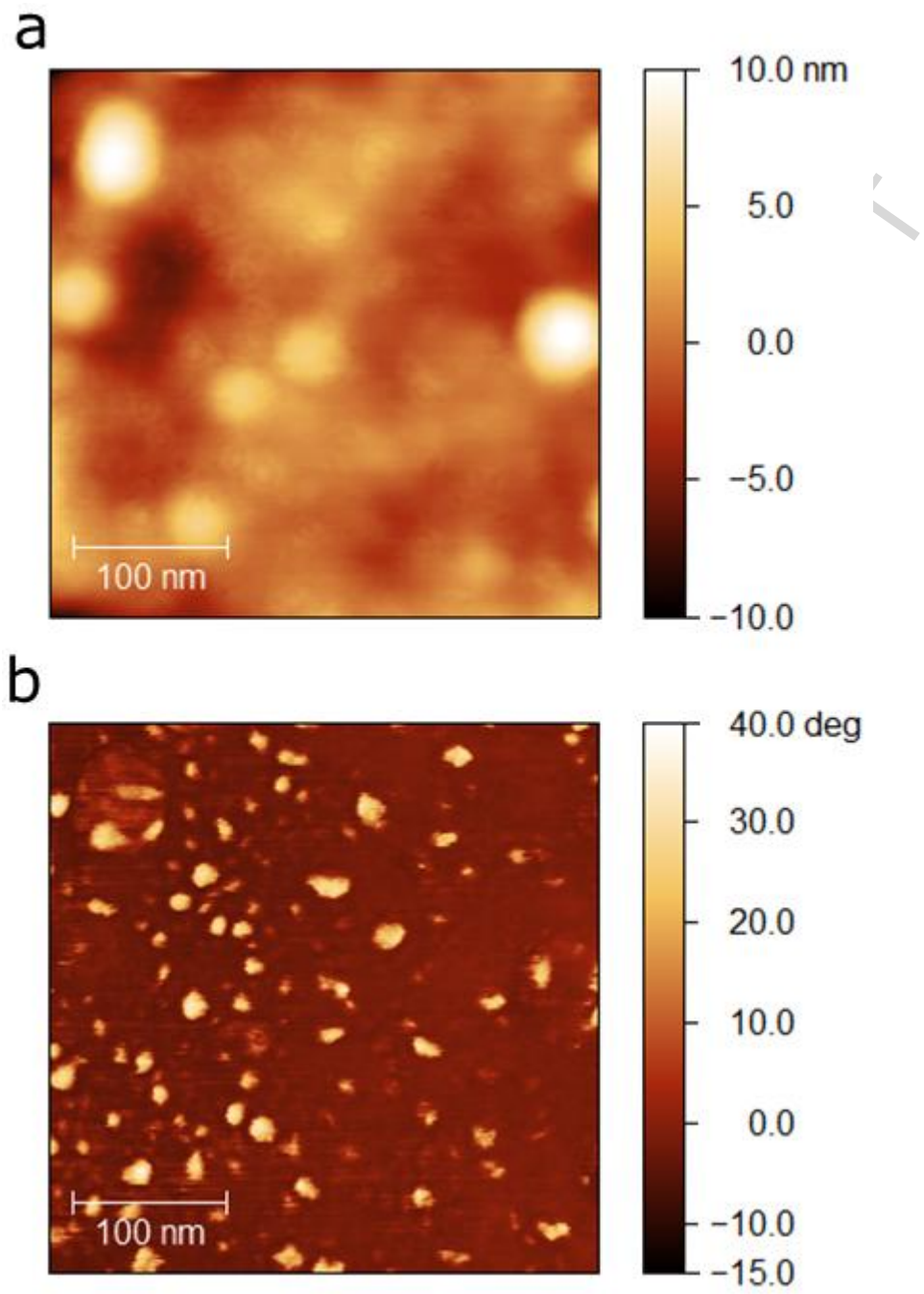

Figure4

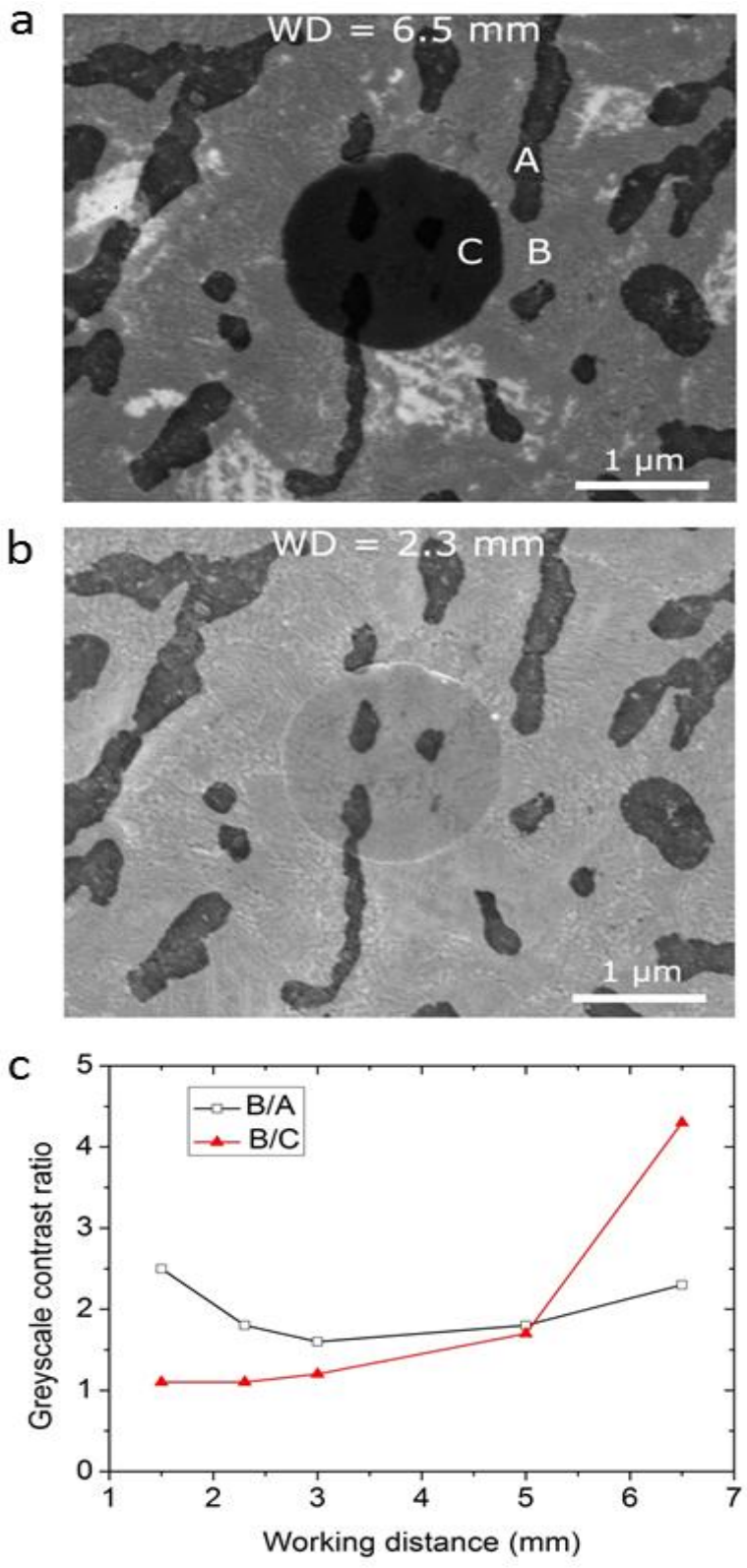
a
WD = 6.5 mm
A
C
B
1 μm
b
WD = 2.3 mm
1 μm
c
B/A
B/C
Greyscale contrast ratio
Working distance (mm)
0
1
2
3
4
5
1
2
3
4
5
6
7

Figure5

Highlights

- Bending of carbon nanodisks is induced by the roughness of the gold substrate.
- Confocal Raman microscopy shows a compressive strain induced in the nanodisks.
- The electron microscopy contrast of nanodisks depends on the working distance.

[1] A. Krishnan, E. Dujardin, M.M.J. Treacy, J. Hugdahl, S. Lynum, T.W. Ebbesen, Graphitic cones and the nucleation of curved carbon surfaces, Nature 388 (1997) 451-454.

[2] S. Lynum, J. Hugdahl, K. Hox, R. Hildrum, M. Nordvik, Production of micro domain particles by use of a plasma process, Patent EP1017622.

[3] S.N. Naess, A. Elgsaeter, G. Helgesen, K.D. Knudsen, Carbon nanocones: wall structure and morphology, Sci. Technol. Adv. Mater. 10 (2009) 065002-1–065002-6.

[4] H. Heiberg-Andersen, A.T. Skjeltorp, K. Sattler, Carbon nanocones: A variety of non-crystalline graphite, J. Non-Cryst. Solids 354 (2008) 5247-5249.

[5] T. Garberg, S.N. Naess, G. Helgesen, K.D. Knudsen, G. Kopstad, A. Elgsaeter, A transmission electron microscope and electron diffraction study of carbon nanodisks, Carbon 46 (2008) 1535-1543.

[6] T. Li, Z. Zhang, Substrate-regulated morphology of graphene, J. Phys. D: Appl. Phys. 43 (2010) 075303-1–075303-7.

[7] S. Scharfenberg, D.Z. Rocklin, C. Chialvo, R.L. Weaver, P.M. Goldbart, N. Mason, Probing the mechanical properties of graphene using a corrugated elastic substrate, Appl. Phys. Lett. 98 (2011) 091908-1–091908-3.

[8] Z. Liu, L. Song, S. Zhao, J. Huang, L. Ma, J. Zhang, J. Lou, P.M. Ajayan, Direct growth of graphene/hexagonal boron nitride stacked layers, Nano Lett. 11 (2011) 2032-2037.

[9] L. De Los Santos Valladares, D. Lee, J. Seo, F.L. Leon, D.A. Bustamante, S. Suzuki, Y. Majima, T. Mitrelias, A. Ionescu, C.H.W. Barnes, Crystallization and surface morphology of Au/SiO2 thin films following furnace and flame annealing, Surf. Sci. 603 (2009) 2978-2985.

[10] A. Serrano, O. Rodríguez de la Fuente, M.A. García, Extended and localized surface plasmons in annealed Au films on glass substrates, J. Appl. Phys. 108 (2010) 074303-1–074303-7.

[11] F. Ding, H. Ji, Y. Chen, A. Herklotz, K. Dörr, Y. Mei, A. Rastelli, O.G. Schmidt, Stretchable graphene: a close look at fundamental parameters through biaxial straining, Nano Lett. 10 (2010) 3453-3458.

[12] T.M.G. Mohiuddin, A. Lombardo, R.R. Nair, A. Bonetti, G. Savini, R. Jalil, N. Bonini, D.M. Basko, C. Galiotis, N. Marzari, K.S. Novoselov, A.K. Geim, A.C. Ferrari, Uniaxial strain in graphene by Raman spectroscopy: G peak splitting, Grüneisen parameters, and sample orientation, Phys. Rev. B 79 (2009) 205433-1–205433-8.

[13] J.E. Lee, G. Ahn, J. Shim, Y.S. Lee, S. Ryu, Optical separation of mechanical strain from charge doping in graphene, Nat. Commun. 3 (2012) 1024-1–1024-8.

[14] F. Tuinstra, J.L. Koenig, Raman spectrum of graphite, J. Chem. Phys. 53 (1970) 1126-1130.

[15] P. Thomas, D. Himmel, J.L. Mansot, W. Zhang, M. Dubois, K. Guérin, A. Hamwi, Friction properties of fluorinated carbon nanodiscs and nanocones, Tribol. Lett. 41 (2011) 353-362.

[16] W. Zhang, M. Dubois, K. Guérin, P. Bonnet, E. Petit, N. Delpuech, D. Albertini, F. Masin, A. Hamwi, Effect of graphitization on fluorination of carbon nanocones and nanodiscs, Carbon 47 (2009) 2763-2775.

[17] J.J. Lander, Auger peaks in the energy spectra of secondary electrons from various materials, Phys. Rev. 91 (1953) 1382-1387.

[18] M. Toth, B.L. Thiel, A.M. Donald, Interpretation of secondary electron images obtained using a low vacuum SEM, Ultramicroscopy 94 (2003) 71-87.

[19] W.J. Yu, Z. Li, H. Zhou, Y. Chen, Y. Wang, Y. Huang, X. Duan, Vertically stacked multi-heterostructures of layered materials for logic transistors and complementary inverters, Nat. Mater. 12 (2013) 246-252.

Figure captions:

Figure 1. AFM image of the gold surface a) before and b) after annealing at 400 ^{o}C. The scale bar is 3 μm in both images.

Figure 2. AFM images of carbon nanodisks a) and c) as-deposited; b) and d) after annealing. Scale bars are 500 nm. Line sections show that the disks are deformed upon annealing as they follow the roughened gold surface. Vertical (*H*) and horizontal (*L*) distances between the marker lines are shown. e-f) Confocal Raman maps measured on the disks in b) and d), respectively. g) Correlation plots (ω_G, ω_D) for disk *1* (blue circles) and disk *2* (white circles). The solid line is the slope if only strain is taken into account, while the dotted line corresponds to shifts due to solely doping effects.

Figure 3. Confocal Raman microscopy performed on the same carbon nanodisk a) before and b) after annealing. The maps show the distribution of the *G* peak centre ω_G. c) Correlation plots (ω_G, ω_D) before (white circles) and after (red circles) annealing. The slopes denoting purely strain (solid line) and doping effects (dotted line) are also plotted. d) Averaged Raman spectra before (black curve) and after (red curve) annealing.

Figure 4. AFM measurements performed on the surface of a carbon nanodisk. a) Topographic and b) phase images from the same area.

Figure 5. FE-SEM images obtained at two different working distances (WD). Regions which give different greyscale contrast are labelled A, B, and C (see the main text). a) WD = 6.5 mm. b) WD = 2.3 mm. c) WD dependent greyscale contrast ratio between the different regions.